Niobium Pentaoxide Thin-Film Gas Sensor for Portable Acetone Sensing

ChemistryEurope

ChemistryEurope
Excellence in Chemistry Research Worldwide

RESEARCH ARTICLE OPEN ACCESS

Tailoring NiO Defectivity to Boost the Electrocatalytic Activity Toward Nitrate Reduction Into Ammonia

Lorenzo Sibella[1] | Andrea Muscatello[1] | Alessandro Padua[1] | Sara Garcia-Ballesteros[1] | Micaela Castellino[1,2] | Antonietta Mancuso[3] | Vincenzo Vaiano[3] | Serena Esposito[1] | Federico Bella[1]

[1]Department of Applied Science and Technology, Politecnico di Torino, Turin, Italy | [2]Center for Sustainable Future Technologies, Istituto Italiano di Tecnologia, Turin, Italy | [3]Department of Industrial Engineering, University of Salerno, Fisciano (Salerno), Italy

Correspondence: Serena Esposito (serena_esposito@polito.it) | Federico Bella (federico.bella@polito.it)

Received: 3 September 2025 | **Revised:** 1 December 2025 | **Accepted:** 7 January 2026

Keywords: ammonia | electrocatalyst | electrochemical nitrate reduction | electrosynthesis | nickel oxide

ABSTRACT

Ammonia is vital for global agriculture, yet its conventional synthesis via the Haber–Bosch process is energy-intensive and environmentally burdensome, contributing ~2% of global CO_2 emissions. Simultaneously, excessive use of ammonia-based fertilizers has led to nitrate pollution in water systems. Electrochemical nitrate reduction (E-NO_3RR) offers a dual solution: mitigating nitrate contamination while enabling decentralized, sustainable ammonia production. Here, we explore nickel oxide (NiO) nanoparticles as efficient, low-cost electrocatalysts for E-NO_3RR, capitalizing on their earth abundance and inherent ability to suppress competing hydrogen evolution. NiO is synthesized via a scalable precipitation method using different ethanol/water solvent ratios to modulate defect density, porosity, and crystallinity. Materials-related differences are probed by thermal, structural, and spectroscopy methods. Electrochemical tests reveal that increasing ethanol content during synthesis enhances defectiveness, correlating with improved Faradaic efficiency and ammonia production rates. This work underscores the critical role of synthetic parameters in tailoring catalytic performance and positions defect-engineered NiO as a promising platform for green ammonia generation via nitrate reduction.

1 | Introduction

The groundbreaking discovery by Fritz Haber in the early 20th century led to a dramatic increase in ammonia production, enabling large-scale fertilizer manufacturing [1, 2]. This advancement significantly boosted agricultural yields and helped meet the growing global demand for food. Today, the Haber–Bosch process remains the dominant industrial method for ammonia synthesis, producing approximately 188 million metric tonnes of ammonia annually [3]. However, despite its efficiency, this process features a considerable environmental footprint, accounting for nearly 2% of global CO_2 emissions due to its high energy demand and reliance on fossil fuels [4]. In response to these concerns, alternative methods for ammonia production have gained attention in recent years [5, 6]. Among them, the electrochemical nitrate reduction reaction (E-NO_3RR) has emerged as a promising approach [7–9]. Nitrates are widely present in water systems, where they pose serious threats to human health [10, 11]. Their prevalence is largely due to the intensive use of nitrogen-based fertilizers, which leads to contamination of both groundwater and surface water bodies [11, 12].

While ammonia production via nitrate electroreduction is limited by their typically low concentration in most wastewater sources, E-NO_3RR is not envisioned as a replacement for the Haber–Bosch process in meeting the global ammonia demand [13–15]. Instead, its primary goal is to convert a harmful pollutant (i.e., nitrate) into a valuable product using renewable electricity, thereby contributing to both environmental remediation and sustainable resource recovery [16–18].

In this scenario, the E-NO_3RR efficiency has a critical dependence on the performance of the electrocatalysts, intrinsically linked to their fundamental electronic and structural characteristics [19, 20].

Lorenzo Sibella and Andrea Muscatello contributed equally to this work.

Within the proposed mechanism for nitrate electroreduction, a range of metals, both noble (e.g., Pd, Pt, Ru, Ag, and Au) and non-noble (e.g., Fe, Co, Ni, and Cu), can exhibit significant catalytic activity due to their partially or fully occupied d-orbitals, which facilitate electron injection into the lowest unoccupied π^* orbitals of nitrate ions [21, 8].

While noble metals universally demonstrate excellent performance when adopted for various electrocatalytic reactions, their high cost and inferior susceptibility restrict their practical, large-scale application. Moreover, the strong affinity of hydrogen species on Pt-group metals can adversely affect the adsorption and conversion of nitrate [22, 23]. To overcome these limitations, research interest has shifted toward developing electrocatalysts based on non-noble metals, which offer advantages in terms of cost-effectiveness and abundance [24]. Among these, nickel stands out in terms of its high earth reserves, affordable availability, good conductivity, magnetic recyclability, and the possibility of a wide variety of nanostructures that make it an ideal candidate for electrochemical reactions [25].

Furthermore, unlike some noble metals, nickel can regulate hydrogenation kinetics, thereby suppressing the competing hydrogen evolution reaction (HER) and enhancing selectivity toward ammonia [26, 27]. The understanding and development of nickel-based nanomaterials therefore represent a preferential research direction for large-scale applications in electrochemical NH_3 synthesis. Nevertheless, while bare nickel metal has indeed shown some activity for nitrate electroreduction, its overall performance is generally not satisfactory [25]. This limitation has driven extensive research into more complex Ni-based systems, including alloys, mixed oxides, Ni-based phosphide, and various composites, which aim to overcome the inherent drawbacks of the single metal by tailoring the catalyst surface properties. It is worth underlying that these catalysts often require intricate synthetic routes involving numerous steps and environmentally detrimental chemicals.

In this scenario, the current literature lacks comprehensive studies on the performance of NiO as a standalone catalyst for E-NO_3RR, prepared through a simplified, greener approach. Thus, in the present work, NiO nanoparticles were synthesized by the precipitation method. This technique was chosen given its cost-effectiveness, simplicity, mild reaction conditions, and the ease of scale-up, all crucial factors for electrocatalytic applications. Specifically, we employed ethanol, water, and various ethanol/water ratios to investigate how solvent composition influences crystallinity and defectivity, and consequently, the catalytic performance of the NiO nanoparticles. To evaluate the performance of each synthesized material in terms of Faradaic efficiency (FE%) and ammonia production rate, electrochemical tests were carried out, specifically chronoamperometry (CA), using an H-type cell equipped with a three-electrode configuration. FE% values exceeding 60% were detected and correlated with synthetic protocols as well as materials properties.

2 | Experimental Section

2.1 | Chemicals and Materials

Nickel(II) nitrate hexahydrate ($Ni(NO_3)_2{\cdot}6H_2O$) was purchased from Supelco with a purity greater than or equal to 99.0%. Sodium hydroxide (NaOH) was purchased from Carlo Erba with a purity greater than or equal to 97.0%. Ethanol absolute (CH_3CH_2OH) was purchased from ITW Reagents, S.R.L., with a purity greater than or equal to 99.8%. All the chemicals were used with no further purification step.

The salts used for the preparation of the electrolyte were potassium nitrate (KNO_3, 99.0%, as the source of NO_3^-) and potassium sulfate (K_2SO_4, 99.0%, as the supporting electrolyte). Ammonium chloride (NH_4Cl, ≥99.5%) was used to prepare the calibration solutions. The reagents used for ammonia detection included sodium salicylate ($C_7H_5NaO_3$, 99.5%), sodium nitroprusside dihydrate ($Na_2[Fe(CN)_5NO]{\cdot}2H_2O$, 99.0%), an aqueous sodium hypochlorite solution (NaClO, 5 wt% active chlorine), sodium citrate dihydrate ($HOC(COONa)(CH_2COONa)_2{\cdot}2H_2O$, ≥99.0%), and sodium hydroxide (NaOH, ≥97.0%). Potassium hydroxide (KOH, 99.0%) and sulfuric acid (H_2SO_4) were used to adjust the pH of each sample. For the preparation of the catalyst ink, NiO nanoparticles, isopropanol ($CH_3CH(OH)CH_3$) or ethanol, and a 5 wt% Nafion perfluorinated resin solution were used. All chemicals and reagents mentioned in this paragraph were purchased from Sigma–Aldrich. A Nafion membrane (Nafion 117 with a thickness of 183 μm, N-117) and a Teflon-coated carbon paper (Toray, 0.19 mm-thick and 20% Teflon in weight) were purchased from Quintech.

The water used in this work was pure water with an 18.2 MΩ cm resistivity, obtained via a Rephile Genie U Ultrapure & RO lab water system.

2.2 | NiO Synthesis

Three distinct samples were synthesized using a chemical precipitation method, adapted from a previously established protocol [28]. The primary modification in this study involved systematically varying the solvent composition during the precipitation process. Specifically, the following solvent systems were employed: 100% deionized water, 32% v/v ethanol/water, 100% ethanol. This controlled variation in solvent composition aimed at exploring its influence on the morphology, crystal structure, and overall properties of the synthesized materials. Further characterizations will elucidate the specific impact of each solvent environment.

In synthetic protocols based only on aqueous medium, 4.35 g (15 mmol) of $Ni(NO_3)_2{\cdot}6H_2O$ were dissolved in 35 mL of water. After stirring for 25 min, 75 mL of a NaOH 0.5 M aqueous solution was added dropwise, and the resulting solution was stirred for 2 h. The greenish gel was then centrifuged, and the resulting precipitate was washed twice with bi-distilled water, followed by one step in ethanol to remove any impurities. The solid was dried overnight at 60°C and then crushed with a mortar to obtain a light green powder, which was finally calcinated in a muffle at 400°C, at a heating rate of 10°C min^{-1} for 1 h. A black NiO powder was finally collected and labeled W100 (W = water, 100 = volume percentage of water in the solution). The synthetic protocol for the sample labeled E32 (E = ethanol, 32 = volume percentage of ethanol in the solution) follows the same steps as the W100, with the exception that 35 mL of ethanol were used in place of the 35 mL of water in the first step. The last sample, labeled as E100 (E = ethanol, 100 = volume percentage of ethanol in the solution), was synthesized as follows: 2 g (6.88 mmol) of $Ni(NO_3)_2{\cdot}6H_2O$ were dissolved in 123 mL of ethanol. After stirring for 25 min, 2.75 mL of a 5 M NaOH solution were added

dropwise, and the resulting solution was stirred for 2 h. The subsequent steps were consistent with the prior synthetic protocols. The flowcharts in Figure 1 summarize the synthetic protocols of sample E32, described in this section. The synthetic protocols for samples W100 and E100 are provided in the Supporting Information (Figure S1a,b).

2.3 | Materials and Electrodes Characterization

X-ray powder diffraction (XRD) was performed on a Philips X'Pert diffractometer equipped with Cu Kα radiation (2θ range = 20°−80°; step = 0.026° 2θ; time per step = 250 s). Lattice parameters and cell volumes were determined by UnitCell Software, while the crystallite size (D) was calculated by Scherrer's equation:

$$D = k\,\lambda\,\beta\cos\theta \tag{1}$$

where k is a constant equal to 0.90, λ is the X-rays wavelength (i.e., 0.154 nm), β is the full width at half maximum, and θ is the half diffraction angle.

N_2 adsorption/desorption isotherms at −196°C were recorded to determine the textural properties of NiO powder. The powder was previously outgassed at 180°C for 3 h to remove water and other atmospheric contaminants using Micrometrics ASAP, 2020Plus. Brunauer–Emmett–Teller method was used to calculate the specific surface area (SSA); the total pore volume (V_p) was determined from the amount of N_2 desorption at $p/p° = 0.98$, the micropore volume (V_{mp}) and the external surface area (S_{ext}) were determined according to the t-plot method. The evaluation of pore size distribution was obtained by using the Barrett–Joyner–Halenda (BJH) method from the desorption branches of the N_2 isotherms.

To monitor the thermal decomposition of the NiO precursor, specifically tracking the conversion from nickel hydroxide to nickel oxide, thermogravimetric analysis (TGA) was performed on STA PT1600 (Linseis instrument, Germany). The curves were recorded in air, increasing the temperature from 25 to 1000°C at a rate of 10°C min^{-1}.

To get insight into the structural features of prepared catalysts, laser Raman spectra were obtained at room temperature with a dispersive MicroRaman (Invia, Renishaw), equipped with a 514 nm laser, in the range 200–1400 cm^{-1}. X-ray photoelectron spectroscopy (XPS) measurements were performed using a PHI 5000 VersaProbe II spectrometer equipped with a monochromatic Al Kα X-ray source. Charge compensation was achieved using a dual system combining low-energy electrons and Ar^+ ions. The conditions used for all survey scans were as follows: energy range 1200–0 eV, pass energy 187.85 eV, step size 0.8 eV, step time 20 ms, and X-rays spot size 100 µm. For high-resolution (HR) spectra, an energy range of 50–20 eV was used, depending on the peak under investigation, with a pass energy of 23.50 eV and a step size of 0.1 eV, step time 50 ms, and X-rays spot size 100 µm. The binding energy scale was referenced to the C–C peak of C 1s at 284.8 eV, attributed to the adventitious carbon. All spectra were analyzed using CasaXPS version 2.3.18 software. The background of each spectrum was subtracted using a Shirley function. Relative atomic concentration values were deduced from the HR spectra using appropriate sensitivity factors.

To investigate the morphological organization of the material once deposited on the carbon support, and to observe any morphological changes after the electrochemical tests, field emission scanning electron microscopy (FESEM) analysis was carried out.

Such an investigation protocol has been guided by recent outcomes in the electrocatalysis field [29–32].

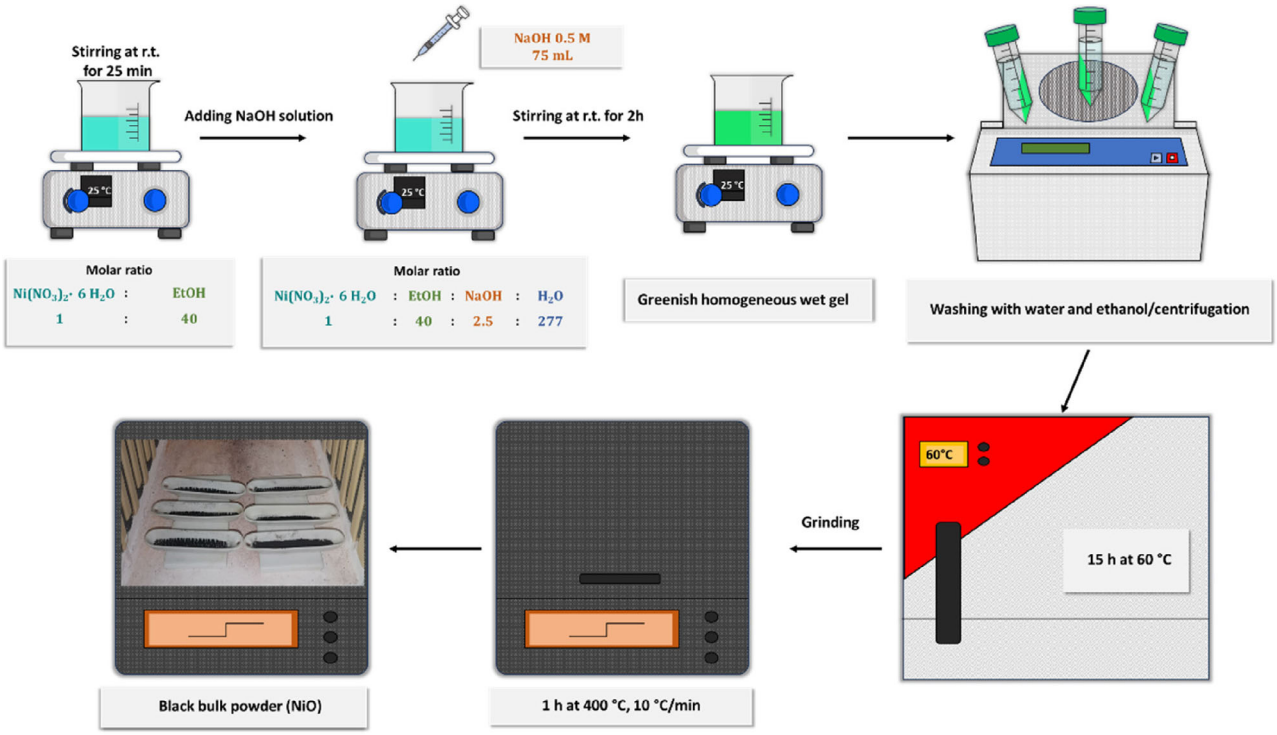

FIGURE 1 | Synthetic protocol of sample E32.

2.4 | Electrochemical Setup

The electrochemical setup consists of an H-type cell (purchased from Laborxing), and all tests were conducted using a three-electrode configuration. A silver/silver chloride (Ag/AgCl) electrode was employed as the reference electrode, and a platinum mesh served as the counter electrode. The working electrode was prepared by depositing an ink onto a Teflon-coated carbon paper, being 0.19 mm-thick (20 wt% poly(tetrafluoroethylene) coated substrate), using an IWATA RG-3L airbrush. The ink was composed of NiO nanoparticles, butanol or isopropanol (or ethanol), and a 5% Nafion solution; the ratio between the ink components followed the procedure reported in the literature [33]. Approximately 95.5% of the solid content was represented by the NiO catalyst, with the remaining 4.5% corresponding to the Nafion binder. To ensure proper dispersion of the ink, an excess amount of ethanol, butanol, or isopropanol was used, and the mixture was ultrasonicated using a SONICS VCX130PB ultrasonic tip as follows: three cycles of 30 s each at 60% or 85% amplitude (with 2 min intervals between cycles) and an additional 20 min sonication at 25% amplitude. After sonication, the ink was transferred into the airbrush and deposited onto the carbon paper substrate, which had been previously placed on a hot plate set to 80°C to facilitate rapid evaporation of the organic solvent. Once the working electrodes were prepared, the H-type cell was assembled. The catholyte and anolyte chambers were filled each with 25 mL of electrolyte composed of K_2SO_4 0.4 M, serving as the supporting electrolyte, and KNO_3 0.1 M as the nitrate source. The two compartments were separated by a Nafion-117 membrane, which had been previously activated by following the procedure reported by Pujiastuti et al., which involves four steps: (1) immerse the membrane for 1 h in H_2O_2 3 wt% solution at 80°C; (2) 1 h rest in ultra-pure water at 80°C; (3) 1 h rest in H_2SO_4 1 M; (4) 1 h rest in ultra-pure water at 80°C [34]. On the cathode side, argon was purged at a flow rate of 50 mL min^{-1} using a Bronkhorst mass flow controller to remove dissolved oxygen from the electrolyte, which could otherwise interfere with the nitrate reduction reaction [11].

A magnetic stirring bar was placed at the bottom of the cathodic chamber and operated at 600 RPM using a magnetic stirrer to minimize mass transport limitations at the surface of the working electrode. To investigate the behavior of the working electrode, and consequently that of the material tested, the cell was connected to a Biologic VSP-300 potentiostat. The electrochemical protocol included the following steps: (1) open circuit potential measurement for 30 min; (2) cyclic voltammetry at a scan rate of 10 mV s^{-1}, within a potential range from −0.2 to −1.8 V versus Ag/AgCl, for a total of six cycles; (3) linear sweep voltammetry (LSV) at a scan rate of 5 mV s^{-1} over the same potential range (−0.2 to −1.8 V vs. Ag/AgCl); (4) CA carried out for 2 h at potentials between −1.0 and −1.6 V, with 0.2 V increments versus Ag/AgCl. The selected range for the CA experiments was defined on the basis of the LSV results. All experiments were performed in triplicate to ensure reproducibility and reliable error estimation.

To accurately quantify the amount of ammonia produced during the electrochemical test, 5 mL aliquots were collected from both the cathodic and anodic chambers prior to the CA step. After that, 10 mL samples were taken from both chambers. This sampling strategy enabled the determination of the net ammonia produced via the nitrate electroreduction process. After quantifying the produced ammonia, the process performance was evaluated by calculating the FE% and the production rate. The former was calculated by:

$$\mathrm{FE\%} = \frac{n F C V}{Q} \tag{2}$$

where n is the number of electrons transferred per molecule of product, F is the Faraday's constant (96485 C mol^{-1}), C is the concentration of product, V is the electrolyte volume, and Q is the total charge passed. As regards the production rate, it was determined by dividing the amount of ammonia produced during the electrochemical test by the duration of the test and the mass of catalyst loaded onto the carbon paper support; its measurement unit was μg h^{-1} mg^{-1}.

2.5 | Ammonia Quantification

The amount of NH_4^+ ions present in the sample before and after the test was determined using the salicylate method [35], which relies on the Berthelot's reaction. Typically, 2 mL of the sample, previously diluted if necessary and adjusted to a pH between 6 and 11 using KOH 5 M or H_2SO_4 1 M – were mixed with 240 μL of salicylate solution ($C_7H_5NaO_3$ 2.75 M and $Na_2[Fe(CN)_5NO]{\cdot}2H_2O$ 0.95 mM) and 400 μL of a reactive solution containing NaClO 0.5 wt%, $HOC(COONa)(CH_2COONa)_2{\cdot}2H_2O$ 340 mM, and NaOH 465 mM. After mixing, the samples were kept in the dark for 45 min to allow the colorimetric reaction to proceed. Subsequently, absorbance was measured at 650 nm using a HITACHI U-500 UV spectrophotometer. To correlate absorbance with concentration, a calibration curve was established using 7 reference points prepared from a NH_4^+ 200 ppm stock solution (NH_4Cl was used as the NH_4^+ source).

3 | Results and Discussion

While precipitation offers a straightforward method for NiO synthesis, achieving controlled material properties remains a challenge. This study specifically aimed at elucidating how the solvent employed during the precipitation step critically impacts the resulting NiO characteristics. The first product obtained following precipitation and subsequent drying was nickel hydroxide. According to the literature, nickel hydroxide displays two distinct polymorphs, i.e., α and β-$Ni(OH)_2$. α-$Ni(OH)_2$ is a hydrated, nonstoichiometric hydroxy-deficient phase, characterized by increased interlayer spacing due to the presence of water molecules intercalated between its layers. These water molecules establish strong hydrogen bonds with hydroxyl groups, causing loss of slab orientation. These phases can accommodate the negative ions present in solution to balance the total charge. α-$Ni(OH)_2$ is unstable, and it is hard to prepare since this phase rapidly changes to the β-form during synthesis or upon storage in a strongly alkaline medium. However, the synthesis route strongly impacts on the preparation of α-$Ni(OH)_2$, and generally harsh conditions are required [36].

Instead, β-$Ni(OH)_2$, a stoichiometric and crystalline phase comprising slabs that exhibit the same orientation, can be obtained by aging the hydroxide gel. This phase is anhydrous, with Van der Waals forces holding the crystalline planes together. A β_{bc} (bad

crystallized) phase has also been documented, with anions included in a more disordered structure [37].

3.1 | TGA

To gain a comprehensive understanding of the thermal decomposition of nickel hydroxide, the first product obtained from the precipitation synthesis, its subsequent conversion into nickel oxide, and to accurately highlight the optimal calcination temperature, a TGA of the precursor hydroxide E100 was systematically performed. The TGA curves (Figure 2a) showed an initial mass loss occurring between 25°C and approximately 200°C. This phase is primarily attributed to the elimination of both adsorbed and intercalated water molecules [38, 39]. Subsequently, a sharp and significant mass decrease is observed, beginning at around 210°C. This thermal event indicates the formation of nickel oxide, with the decomposition of any residual nitrates potentially contributing to the mass loss in this temperature range. The last weight loss, for all samples at >300°C, is linked to the removal of the excess oxygen in Ni_xO_y species (black powder) to a stoichiometric NiO (green powder) [40, 41]. This finding aligns with established literature, which identifies the cubic NiO phase as forming within the 300–900°C calcination range. Specifically, calcination in air at 400°C is optimal for achieving a NiO phase with controlled cationic defectivity while limiting sintering. The TGA curves for samples E32 and W100 (data not reported) showed no significant differences compared to those of sample E100.

3.2 | Powder XRD Patterns

XRD was performed only on one representative sample of $Ni(OH)_2$, namely precursor hydroxide E100, as the primary focus of this study was the structural characterization of the calcined NiO products. The diffractogram of precursor hydroxide of E100 is shown in Figure 2b. The observed diffraction peaks exhibit a good correspondence with the β-$Ni(OH)_2$ phase (JCPDS card no. 74-2075), specifically at 2θ values of 33.0° (100) plane, 38.4° (101) plane, 51.9° (102) plane, 59.0° (110) plane, 62.6° (111) plane, 69.5°, and 72.7°. However, the significant broadening of these peaks indicates a low degree of crystallinity within the sample. The presence of two distinct peaks at d-values of 5.75 Å and 4.35 Å, which do not correspond to characteristic reflections of

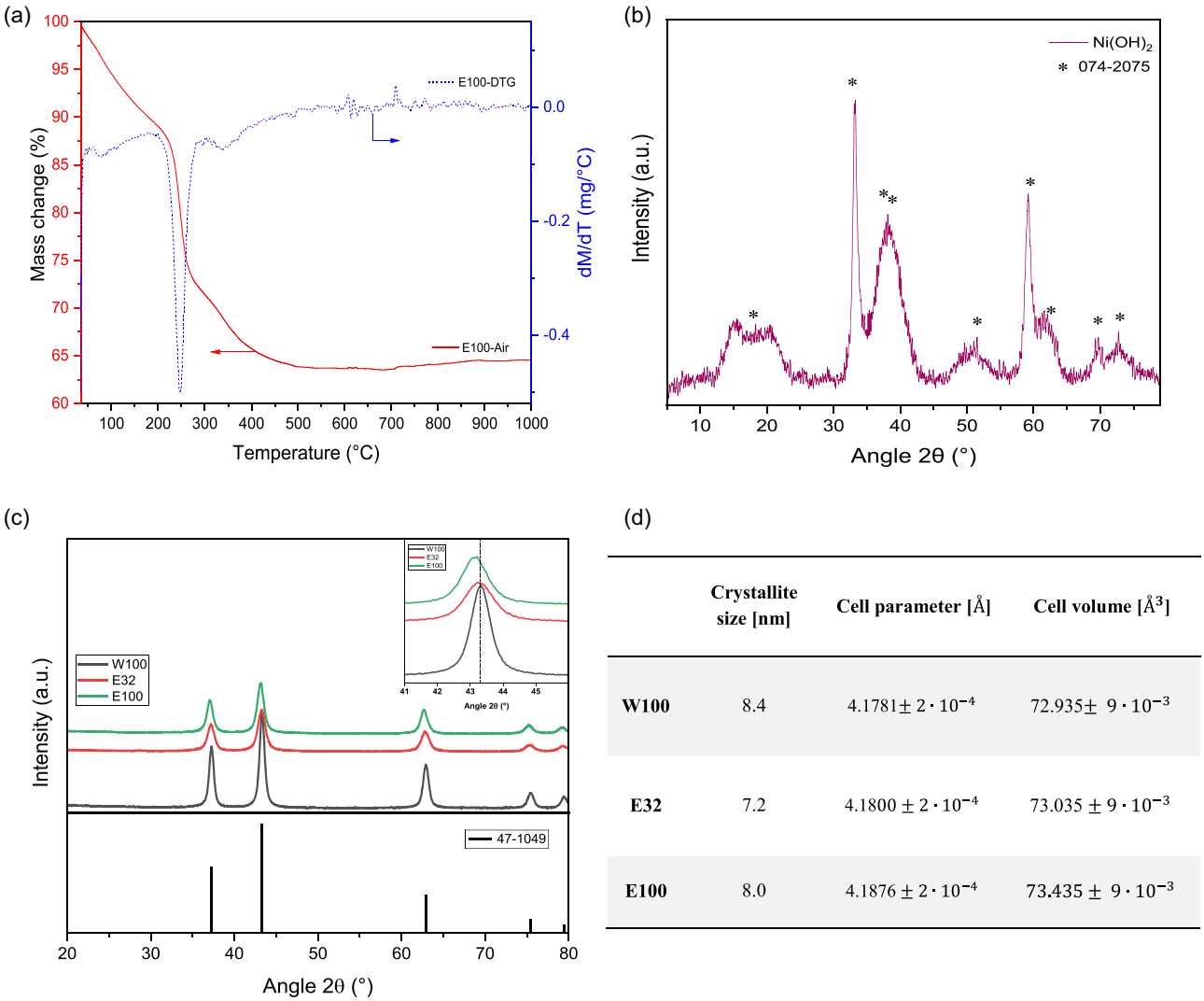

(d)

	Crystallite size [nm]	Cell parameter [Å]	Cell volume [Å^3]
W100	8.4	$4.1781 \pm 2 \cdot 10^{-4}$	$72.935 \pm 9 \cdot 10^{-3}$
E32	7.2	$4.1800 \pm 2 \cdot 10^{-4}$	$73.035 \pm 9 \cdot 10^{-3}$
E100	8.0	$4.1876 \pm 2 \cdot 10^{-4}$	$73.435 \pm 9 \cdot 10^{-3}$

FIGURE 2 | (a) TGA curve (red) and DTG curve (blue) in air of precursor hydroxide E100; (b) Powder XRD pattern of precursor hydroxide E100. The asterisks refer to the JCPDS card no. 74-2075; (c) Powder XRD patterns of NiO W100, E32, and E100 samples compared with the reference pattern of cubic NiO (JCPDS card no. 47-1049). (d) Crystallite size and cell parameter of NiO W100, E32, and E100 samples.

either α-Ni(OH)$_2$ or β-Ni(OH)$_2$, suggests the formation of a poorly crystallised β-Ni(OH)$_2$ phase containing minor amounts of the α-Ni(OH)$_2$ polymorph. This observation indicates an impure or structurally disordered material [37].

Figure 2c shows the XRD plot of W100, E32, and E100 samples after calcination at 400°C in air at a heating rate of 10°C min^{-1} for 1 h. All diffractograms clearly show a series of well-defined diffraction peaks, which exhibit excellent correspondence with the characteristic reflections of the face-centered cubic NiO phase (JCPDS card no. 47-1049). Specifically, the observed peaks are prominently located at 2θ values of approximately 37.3°, corresponding to the (111) crystallographic plane, 43.3° for the (200) plane, 62.9° for the (220) plane, 75.4° for the (311) plane, and 79.4° for the (222) plane. The sharp and intense nature of these peaks indicates the formation of a highly crystalline NiO structure in all samples after thermal treatment [42].

Despite its idealized 1:1 stoichiometry, NiO is typically a nonstoichiometric p-type oxide, characterized by a slight oxygen excess and a consequent deficiency in nickel cations. The presence of Ni^{2+} vacancies within the NiO lattice leads to the formation of charge-compensating Ni^{3+} ions (or electron holes) to maintain electroneutrality [40, 41]. This can be expressed in Kröger–Vink's notation as:

$$2Ni^{2+} + \frac{1}{2}O_2 \leftrightarrow O_0 + Vi''_{Ni} + 2Ni^{3+}$$

The crystallite size and cell parameters of W100, E32, and E100 samples are summarized in Figure 2d. The diffractogram of W100 sample indicates a higher degree of crystallinity, as evidenced by its larger crystallite size. Notably, a progressive shift of the diffraction peaks toward lower 2θ values is observed, moving sequentially from sample W100, through E32, and ultimately to E100. This shift, which is directly correlated with the unit cell parameter, suggests a higher degree of cationic defectiveness in E100, likely due to excess oxygen in the lattice [40].

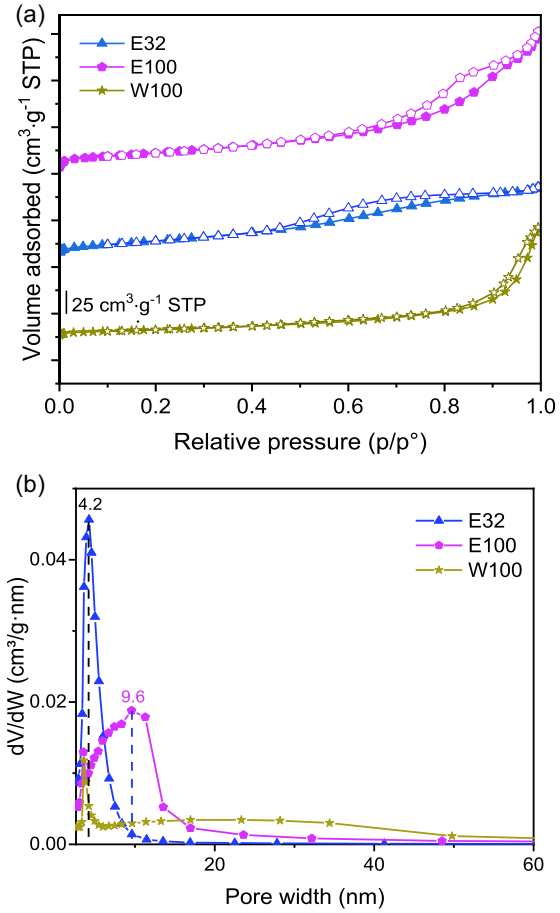

FIGURE 3 | (a) N_2 adsorption–desorption isotherms of W100, E32, and E100 samples; (b) BJH pore size distributions of W100, E32, and E100 samples. The evaluation of pore size distribution was obtained by using the BJH method from the desorption branches of the N_2 isotherms. Full symbols indicate adsorption, while empty symbols refer to desorption.

3.3 | N_2 Physisorption

The N_2 adsorption/desorption isotherms of W100, E32, and E100 samples are shown in Figure 3a. The analysis of the isotherm shapes indicates that they are of type IV(a), where the hysteresis is produced by capillary condensation in mesopores, the width of which is wider than ca. 4.0 nm [43]. Although the characteristic inflection point indicating the completion of the monolayer can be seen at $p/p° = 0.01$ in the isotherms of E32 and E100 samples, this feature is completely absent in the isotherm of W100 sample. The shape of the hysteresis loop allows for the determination of the pore structure. According to the IUPAC classification, the hysteresis of W100 sample can be categorized as type H1, which is typically associated with porous materials that exhibit a narrow distribution of relatively uniform, cylindrical-like pores [44]. The hysteresis of the E32 sample can be associated with type H2(b), which is typical of ink-bottle pores with a wide distribution of neck widths [43]. However, determining the hysteresis type of the E100 sample is not straightforward. Due to the presence of an inflection point in the desorption branch of the hysteresis, the association with a type H3(b) was considered, where type H3(a) is the one defined in the IUPAC report as H3 [45]. As regards pore shape, we can hypothesize a complex structure resembling an ink bottle with a modified neck. Figure 3b shows the pore size distributions of W100, E32, and E100, which were calculated using the BJH method from the desorption branches of the N_2 isotherms. While W100 sample was characterized by a wide distribution in all mesopore ranges with a sharp peak centered at 3.6 nm, E32 showed a narrow pore size distribution centered at 4.2 nm, whereas E100 had a wider distribution across the 2.6–30 nm range, centered at 9.6 nm. Table 1 lists the textural properties of the three samples. It is evident that precipitation in a hydroalcoholic solution has a significant impact on the specific area values: W100 sample had the lowest surface area and no micropores surface area was detected by applying the t-plot method (y-intercept = 0), while E32 had a slightly higher surface area than E100, and both the t-plot curves highlighted the presence of micropores (y-intercept $\neq$ 0). The micropore surface area accounts for 10% of the calculated SSA value for E32 and 5.6% of the calculated SSA value for E100.

3.4 | Raman Spectra of NiO Powder Samples

Figure 4 shows the Raman spectra of NiO powder samples synthesized via different protocols, revealing characteristic vibrational features associated with the cubic NiO phase. All samples exhibited a

TABLE 1 | Textural properties calculated from N_2 physisorption.

Samples	SSA, $m^2\ g^{-1}$	Micropore volume, $cm^3\ g^{-1}$	External surface area, $m^2\ g^{-1}$	Total pore volume, $cm^3\ g^{-1}$
W100	39.8	—	39.8	0.175
E32	85.7	$1.7 \cdot 10^{-3}$	75.6	0.122
E100	82.4	$5.9 \cdot 10^{-4}$	77.6	0.224

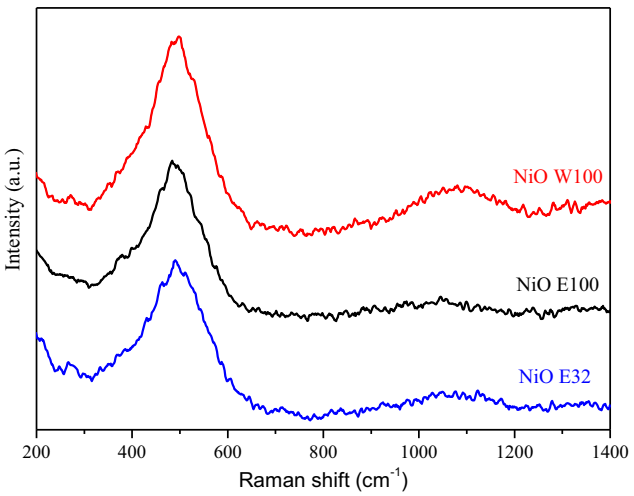

FIGURE 4 | Raman spectra of NiO W100, E32, and E100 samples.

prominent longitudinal optical (LO) phonon mode centered at around 500 cm^{-1}, with very similar intensity and shape, indicating that the primary lattice vibrations of NiO with a rocksalt-type structure [46, 47] are preserved regardless of the preparation route. However, a distinct difference is observed in the second-order 2LO band near 1100 cm^{-1} [48], which is intense in W100, weakly visible in E32, and nearly absent in E100. Since the 2LO band is enhanced in well-ordered and strain-free lattices, its intensity serves as a sensitive indicator of crystallinity and lattice quality [48, 49].

These spectroscopic findings are in good agreement with the XRD data, particularly with respect to the angular position of the diffraction peaks. A clear shift of the main reflections toward lower 2θ values was observed in the E100 sample, while W100 sample showed peaks closer to the standard reference pattern (i.e., JCPDS 47-1049). The shift in E100 indicated a slight lattice expansion, which was also confirmed by the refined lattice parameter ($a = 4.1876$ Å), larger than those of W100 and E32. Lattice expansion is often associated with the presence of defect sites, or internal strain, all of which can contribute to the suppression of the 2LO feature in the Raman spectrum. Conversely, the absence of a significant peak shift in W100 sample suggested a well-ordered, relaxed lattice, in agreement with the stronger second-order Raman signal. Overall, the correlation between the XRD peak shift and the 2LO Raman band intensity supported the interpretation that W100 sample was the most structurally ordered sample, while E100 exhibited the most significant lattice distortion.

3.5 | XPS Spectra of NiO Powder Sample

To gain insight into how the different synthetic conditions influence the surface chemistry and electronic structure of the NiO materials, XPS was employed to analyze the Ni and O environments as well as the valence-band features. Particular attention was given to oxygen stoichiometry and defect-related electronic states, as these factors are expected to strongly influence the catalytic behavior.

From the survey spectra (see Figure 5), we can see the presence of Ni, O, and C, the latter related to environmental contamination by adventitious C. Relative atomic concentration values were evaluated, instead, from the HR spectra of the C 1s, O 1s, and Ni 2p regions, to distinguish between the amount of O related to C bonds or to Ni oxide. These values, along with the oxide/Ni ratios, are reported in Table 2. A clear trend is observed in the amount of Ni, with the lowest value for W100 (35.8 at%), going from E32 (37.6 at%) to the highest value for E100 (41.5 at%). At the same time, a trend is also observed in the oxide/Ni ratios: the highest value for W100 (1.37), a decreasing one for E32 (1.28), up to E100 (1.11), for which the lowest value is recorded.

The Ni $2p_{3/2}$ region (850–865 eV) (see Figure 6a) was analyzed following the procedure of Biesinger et al. [50] and Grosvenor et al. [51]. A Shirley background was subtracted, and the peaks were fitted with a mixed Gaussian–Lorentzian (GL(30)) line shape. The set of curves that best fits the shape of the spectra is the one reported for NiO (see Figure 6), for all the samples. The Ni 2p region is dominated by strong multiplet splitting and satellite structure, which makes it relatively insensitive to small variations in oxygen deficiency, subtle changes in Ni^{2+}/Ni^{3+} ratio, local bonding distortions, carrier density, and small shifts in electronic structure. Therefore, several samples with different defectivity or conductivity can still display almost identical Ni 2p envelope [52], as in our case. To further investigate the

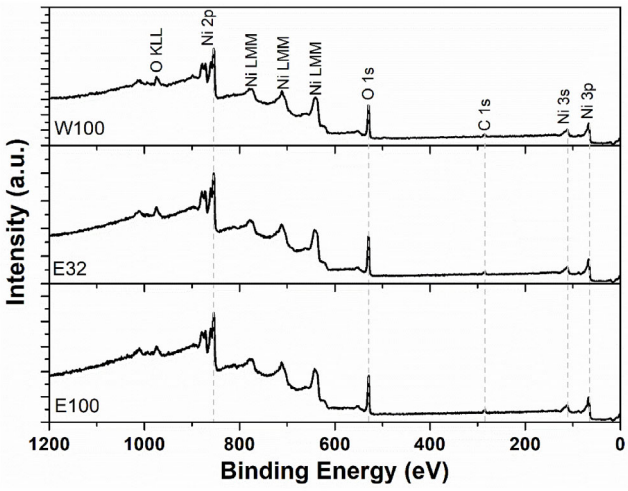

FIGURE 5 | XPS survey scans for W100, E32, and E100 samples.

TABLE 2 | XPS data related to the relative atomic concentration (at%) of samples W100, E32, and 100, together with O 1s regions deconvolution results and modified Auger parameter (MAP), calculated for each of the three samples.

Sample	Relative atomic concentration, at.%				
	C 1s	O 1s		Ni 2p	Ox/Ni
		Bonded with C	Metal oxide		
W100	10.8	4.2	49.2	35.8	1.37
E32	10.5	3.9	48.0	37.6	1.28
E100	9.7	2.8	46.0	41.5	1.11
	O 1s deconvolution results, %				
	O from lattice		O defects	O bonded to C	
W100	71.1		21.0	7.9	
E32	66.4		26.1	7.5	
E100	72.2		22.2	5.6	
	MAP, eV				
	Ni $2p_{3/2}$		Ni LMM	MAP	
W100	853.4		642.3	1697.7	
E32	853.3		642.5	1697.4	
E100	853.3		642.4	1697.5	

oxidation state of Ni oxide, we also analyzed the Auger region of the Ni LMM (not shown), which allowed us to calculate the position of the maximum peak. This value, combined with the position of the Ni $2p_{3/2}$ peak, allows us to calculate the MAP, which is highly sensitive to the average oxidation state of the sample. In our case, as reported in Table 2, the values obtained for the three samples, ranging from 1697.4 to 1697.7 eV, are in agreement with the value reported in the literature for NiO, which corresponds to 1697.7 eV [53].

The O 1s spectra (526–536 eV) were similarly fitted with components corresponding to lattice oxygen (O^{2-}, ~529 eV) and oxygen vacancies or defect-related species (~531.0 eV) (see Figure 6b). The relative % for each component has been reported in Table 2, together with the percentage of O bound to C, as deduced from the deconvolution of the C 1s peak (not reported).

The last region studied was the valence band (see Figure 7). Based on the shape of the curves for the three samples, which were all very similar, they resemble those reported in the literature for NiO, which significantly differs from the VB of, for example, NiOOH [54]. However, it should be noted that, while the valence band maximum (VBM) value for NiO reported in the literature lies in a range of 1.0–1.5 eV below the Fermi level (E_F) for high-quality stoichiometric NiO, the VB of our NiO is significantly different, as it is very close to zero eV. When the VBM and E_F nearly overlap (difference <0.2 eV), the material behaves

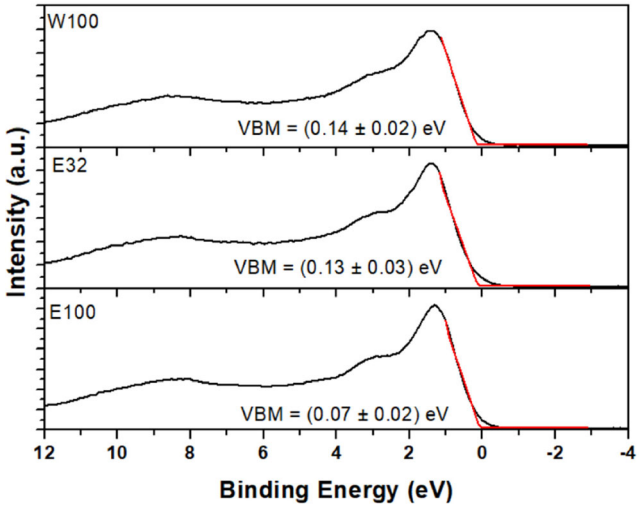

FIGURE 7 | XPS valence band regions for all three samples. The VBM has been calculated by means of the "step-down" function, together with its uncertainties, thanks to Monte Carlo simulations. The final values are reported in each region.

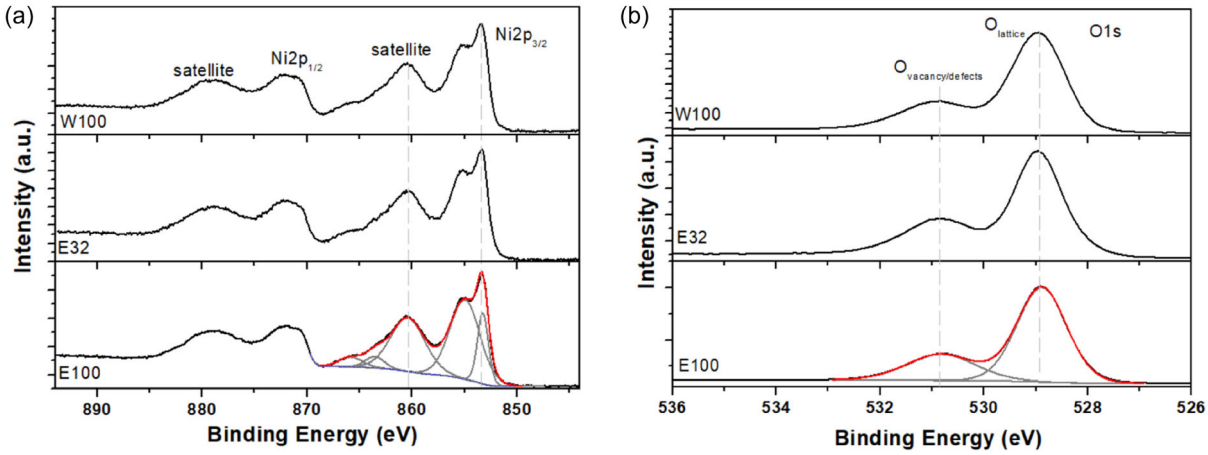

FIGURE 6 | XPS (a) Ni 2p and (b) O 1s regions for all three samples. In the E100 graphs, a deconvolution procedure, following Biesinger et al. [50], has been applied and reported.

as a degenerate p-type semiconductor or even semimetal-like NiO_x [55]. This often occurs in NiO with high Ni^{3+} content (due to Ni vacancies or oxidative treatments), so that the valence band is filled up to E_F by Ni 3d holes. This electronic structure facilitates faster charge transport and easier electron donation. We then calculated the VBM values using the CasaXPS "step-down" function and calculated the uncertainty on the resulting measurement using the associated Monte Carlo simulation. The resulting values are shown in Figure 7. As we can see, there is a trend showing how the VBM moves toward the E_F starting from the W100 sample, to arrive at the E100 sample, which has the value closest to 0 eV. Values in the range 0.0–0.3 eV are usually associated with Ni-rich or highly defective NiO_x [56]. Such electronic structure modification can facilitate charge transfer during the electrochemical nitrate reduction reaction, contributing to the higher ammonia yield observed.

Thus, although the Ni 2p spectra of W100, E32, and E100 appear nearly identical, reflecting the limited sensitivity of the Ni 2p region to subtle defect-induced electronic changes, differences emerge in the valence band and O 1s regions. A progressive shift of the VBM toward the Fermi level is observed as the O/Ni ratio decreases from W100 (1.37) to E32 (1.28) and E100 (1.11) (see Table 2). This correlation indicates that increasing oxygen deficiency drives the formation of defect-related states and enhances Ni 3d–O 2p hybridization at the valence-band edge [52]. As a result, the electronic bandgap effectively narrows and the density of states near the Fermi level increases, consistent with a transition from more insulating (W100) to more conductive and defect-rich behavior (E100). These electronic-structure modifications, rather than changes in the Ni 2p signature, are the key factors explaining the enhanced catalytic activity of E100.

3.6 | Electrochemical Activity Toward E-NO_3RR

To obtain electrodes homogeneously coated with the active materials under investigation, the ink preparation process was optimized, as detailed in the *"Text S1. Ink preparation and optimization"* section of the Supporting Information. The final formulation employs isopropanol as the solvent, since, as it can be seen in Figure S2 and Table S1, it guarantees better dispersion of the material and therefore better performance, and ultrasonication at 85% of the maximum amplitude. Once a suitable ink preparation protocol was established, allowing for homogeneous material dispersion on the electrodes, the performances of W100, E32, and E100 samples were assessed. However, the W100 sample, as well as the data obtained from the electrochemical tests, exhibited poor reproducibility, as evidenced in Figure S3 and Table S2 and further explained in the Supporting Information. Therefore, subsequent investigations focused on samples E32 and E100. Based on the physicochemical characterizations discussed in the previous sections, it is evident that the E100 sample possesses a higher degree of structural defects compared to E32, a feature that could positively affect its selectivity. As illustrated in Figure 8, at the optimal potential of −1.4 V versus Ag/AgCl, the average FE% for E32 was approximately 47 ± 7%, whereas for E100 it reached about 61 ± 9.9%. These findings suggest that E100 exhibits a greater selectivity toward the target reaction. Moreover, Figure 8 clearly shows that the FE% values obtained at the other tested potentials were significantly lower than those achieved at the optimal potential of −1.4 V versus Ag/AgCl. An increase in the applied potential clearly

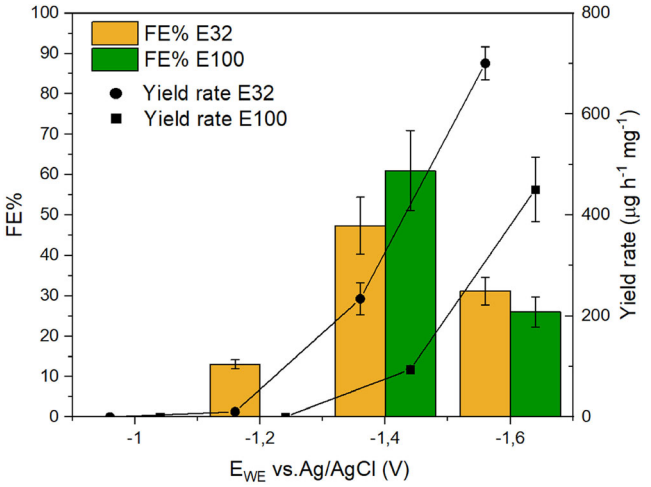

FIGURE 8 | Average FE% and ammonia production rate values for NiO E32 and E100 samples, tested over a potential range from −1.0 to −1.6 V versus Ag/AgCl with an incremental step of 0.2 V.

enhances the ammonia production rate, as observed in a similar system in the literature [57]. Nevertheless, in this system, higher selectivity toward the desired product is considered more relevant than a mere increase in production.

The LSV curves show a clear increase in current density and a positive shift of the onset potential in the presence of NO_3^-, indicating efficient catalytic activity for the E-NO_3RR of both E32 and E100 (Figure 9a,c). To further confirm the higher selectivity of E100, the first derivative of the LSV curves was calculated, and the onset potential was defined as the point beyond which the derivative consistently assumes positive values. From this, ΔE was defined as the difference between the onset obtained in the presence and in the absence of NO_3^-. As it can be observed in Figure 9b,d, ΔE is greater for E100 than for E32, providing additional evidence of its improved selectivity.

3.7 | Electrode Characterization

To evaluate potential morphological changes induced by the electrochemical test, the electrode surfaces were characterized before and after the E-NO_3RR process using Raman spectroscopy and FESEM analysis.

Figure 10 compares the Raman spectra of the carbon support (bare carbon paper) with those of the NiO-loaded electrodes, both in their pristine and post-electrochemical states. All electrodes were prepared by depositing NiO powders (E32, E80, E100, and W100) onto the conductive carbon substrate.

The Raman spectrum of the uncoated carbon paper reveals the characteristic G band (~1580 cm^{-1}), associated with graphitic (sp^2-type) carbon, and a prominent feature at approximately 2700 cm^{-1}, corresponding to the 2D band (also known as the G′ band), a second-order overtone of the D band resulting from a double-resonance scattering process [58, 59]. Upon deposition of the NiO powders onto carbon paper, the resulting composite electrodes exhibit Raman spectra in which the NiO vibrational features are superimposed on the strong background signals from the carbon support. In the pristine electrodes, the NiO signal in the low-Raman shift region remains discernible, though reduced in intensity due to the

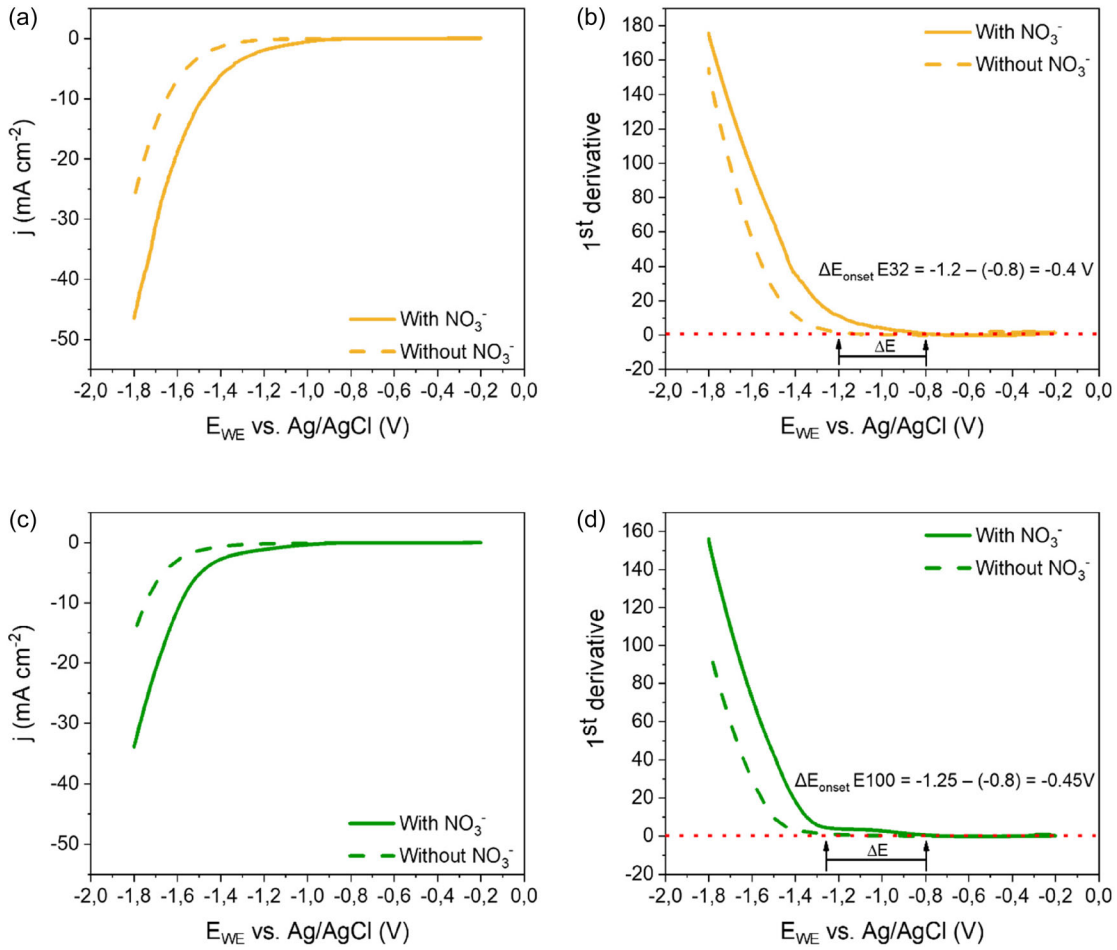

FIGURE 9 | Comparison between LSV measurements recorded with and without nitrate ions in the electrolyte, using (a) E32 and (c) E100 samples, respectively, as the active material. The first derivative of the curve, employed to identify the onset potential of E32 (b) and E100 (d) in both conditions, is also shown.

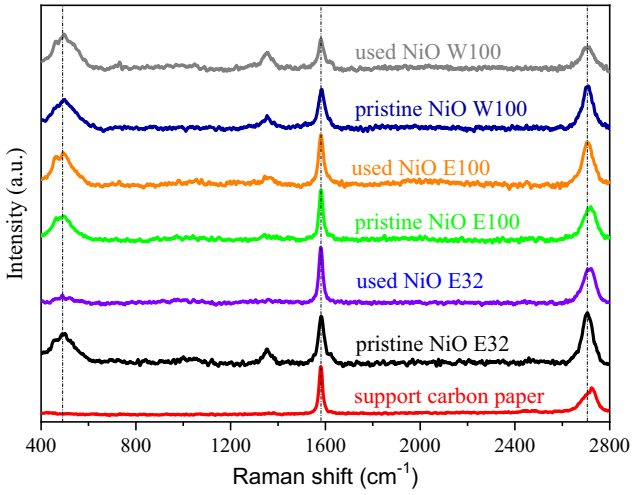

FIGURE 10 | Raman spectra of support carbon paper and NiO-coated carbon electrodes (before and after the E-NO_3RR experiment).

dominance of the carbon Raman response. The presence of this feature confirms the successful deposition of the NiO phase onto the carbon support. No significant shifts or changes in the carbon bands are observed, indicating that the electrode fabrication process does not induce substantial structural degradation in the carbon matrix.

After electrochemical testing, distinct modifications are observed in the Raman spectra of the electrodes, particularly in the low-Raman shift region associated with NiO vibrations (500–600 cm^{-1}). For the E32 electrode, the NiO band significantly weakened and broadened, suggesting a pronounced loss of structural order or possible leaching of the NiO phase under electrochemical conditions. In contrast, for E100 and W100, the main NiO band remained clearly detectable, though slightly broadened, indicating that the NiO framework was largely preserved. Notably, both E100 and W100 also exhibited the emergence of a new band at around ~480 cm^{-1}, which is not present in the pristine samples. This newly developed band is consistent with Raman-active modes attributed to nickel oxyhydroxide (NiOOH) [60]. The coexistence of the original NiO signal with the emerging NiOOH feature suggests partial transformation, rather than complete NiO phase conversion. These observations indicate that the W100 and E100 electrodes undergo a controlled electrochemical evolution, involving the formation of redox-active NiOOH species. Notably, the D and G bands of carbon remain prominent across all tested electrodes, with only marginal broadening, indicating that the carbon support retains its structural integrity throughout the electrochemical treatment. However, minor changes in the D/G intensity ratio may reflect slight increases in surface disorder or defect generation due to oxidative stress.

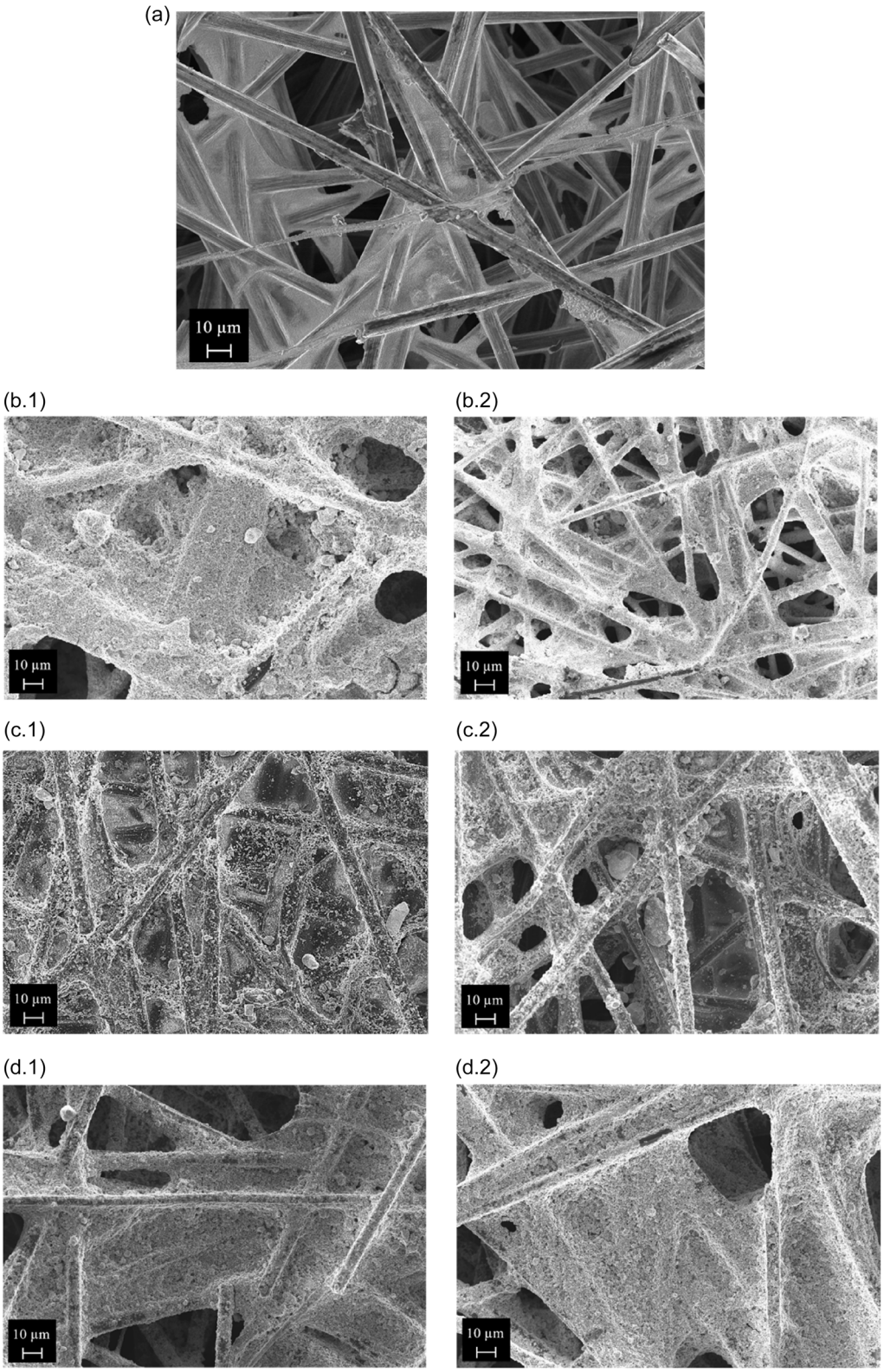

FIGURE 11 | FESEM micrographs for: (a) pristine carbon paper; (b) carbon paper coated with W100 (b.1) before and (b.2) after electrochemical testing; (c) carbon paper coated with E32 (c.1) before and (c.2) after testing; (d) carbon paper coated with E100 (d.1) before and (d.2) after testing.

Figure 11 shows the FESEM micrographs of pristine carbon paper and of the electrodes before and after electrochemical testing, all acquired at the same magnification. The fibrous structure of pristine carbon paper without any deposited material is visible in Figure 11a. After deposition, a more homogenous distribution of the material is observed for E32 (Figure 11c.1) and E100 (Figure 11d.1) compared to W100 (Figure 11b.1), where some aggregates are visible, indicating a weaker ink dispersibility. Finally, the images after the electrochemical testing (Figure 11b.2,c.2,d.2) demonstrate that the morphology of W100, E32, and E100 remains essentially

unchanged, confirming the structural stability of the electrodes under the applied electrochemical conditions.

4 | Conclusion

This study highlights how the choice of solvent during the precipitation synthesis of NiO significantly affects the defectivity, pore size distribution, crystallite size, and cell parameter of the resulting material. By comparing three different samples, W100, E32, and E100, synthesized using water, a water/ethanol mixture, and ethanol, respectively, it was shown that both defectiveness and textural properties are strongly dependent on the solvent employed. Among the samples, E100 exhibited the highest degree of lattice distortion and a broader pore size distribution, features which correlated with enhanced selectivity toward nitrate electroreduction, as confirmed by both electrochemical testing. Conversely, W100, although more crystalline and structurally ordered, suffered from poorer ink dispersibility and reduced reproducibility in electrochemical performance. Furthermore, the results underline the critical role of ink formulation in ensuring electrode homogeneity and performance consistency. By optimizing the solvent and ultrasonication amplitude during ink preparation, a significant improvement in the material dispersion was detected, leading to a homogeneous deposition onto the carbon support. This is a fundamental step to avoid variation coming from the setup and ensure a proper comparison between the catalytic activity of the materials. Overall, this work demonstrates that fine-tuning both the synthesis parameters and the ink deposition process can substantially enhance the performance of NiO-based catalysts in electrochemical nitrate reduction. Future studies will focus on systematically evaluating the effect of each ink formulation parameter and exploring the long-term stability of the most promising materials.

Author Contributions

Lorenzo Sibella: data curation: (lead), investigation: (lead), methodology: (equal), writing the European Union's Horizon 2020 research and innovation program – original draft: (lead). **Andrea Muscatello:** data curation: (lead), investigation: (equal), methodology: (equal), writing – original draft: (lead). **Alessandro Padua:** data curation: (equal), investigation: (equal), methodology: (supporting), writing – review & editing: (equal). **Sara Garcia-Ballesteros:** conceptualization: (equal), funding acquisition: (supporting); methodology: (equal), supervision: (equal), writing – review & editing: (lead). **Micaela Castellino:** methodology: (equal), writing – review & editing: (equal). **Antonietta Mancuso:** data curation: (supporting); investigation: (supporting), writing review & editing: (equal). **Vincenzo Vaiano:** funding acquisition: (supporting), investigation: (supporting), methodology: (supporting), writing – review & editing: (supporting). **Serena Esposito:** conceptualization: (lead), investigation: (supporting), methodology: (equal), project administration: (lead), supervision: (lead), writing – review & editing: (lead). **Federico Bella:** conceptualization: (lead), project administration: (lead), resources: (lead), supervision: (lead), writing – review & editing: (lead).

Acknowledgments

This project has received funding from the European Research Council (ERC) under the European Union's Horizon 2020 research and innovation program (grant agreement No. 948769, project title: SuN_2rise). The project was also supported by the European Union's Horizon 2020 research and innovation programme under the Marie Skłodowska–Curie grant agreement no. 101107906.

Funding

This study was supported by the European Union's Horizon 2020 research and innovation program (ID 948769 and 101107906).

Conflicts of Interest

The authors declare no conflicts of interest.

Data Availability Statement

The data that support the findings of this study are available from the corresponding author upon reasonable request.

References

1. J. A. Renaissance Faria, "Renaissance of Ammonia Synthesis for Sustainable Production of Energy and Fertilizers," *Current Opinion in Green and Sustainable Chemistry* 29 (2021): 100466, https://doi.org/10.1016/j.cogsc.2021.100466.

2. J. Lim, C. A. Fernández, S. W. Lee, and M. C. Hatzell, "Ammonia and Nitric Acid Demands for Fertilizer Use in 2050," *ACS Energy Letters* 6 (2021): 3676–3685, https://doi.org/10.1021/acsenergylett.1c01614.

3. N. Erfani, L. Baharudin, and M. Watson, "Recent Advances and Intensifications in Haber-Bosch Ammonia Synthesis Process," *Chemical Engineering and Processing - Process Intensification* 204 (2024): 109962, https://doi.org/10.1016/j.cep.2024.109962.

4. J. Humphreys, R. Lan, and S. Tao, "Development and Recent Progress on Ammonia Synthesis Catalysts for Haber–Bosch Process," *Advanced Energy and Sustainability Research* 2 (2021): 2000043, John Wiley and Sons Inc, https://doi.org/10.1002/aesr.202000043.

5. A. M. O. Mohamed, I. G. Economou, and Y. Bicer, "Navigating Ammonia Production Routes: Life Cycle Assessment Insights for a Sustainable Future," *Current Opinion in Green and Sustainable Chemistry* 49 (2024): 100947, https://doi.org/10.1016/j.cogsc.2024.100947.

6. Y. Shi, H. Li, X. Liu, et al., "Energy-Driven Ammonia Production for Sustainable Development Goals," *Chem* 10 (2024): 2636–2650, https://doi.org/10.1016/j.chempr.2024.06.014.

7. S. Giddey, S. P. S. Badwal, and A. Kulkarni, "Review of Electrochemical Ammonia Production Technologies and Materials," *International Journal of Hydrogen Energy* 38 (2013): 14576–14594, https://doi.org/10.1016/j.ijhydene.2013.09.054.

8. Md M. Islam, S. M. Abu Nayem, S. S. Shah, Md Z. Islam, Md A. Aziz, and A. J. Saleh Ahammad, "Electrochemical Selective Nitrate Reduction: Pathways to Nitrogen and Ammonia Production," *The Chemical Record* 25 (2025): e202400206, https://doi.org/10.1002/tcr.202400206.

9. M. Ahmed, C. Wang, Y. Zhao, et al., "Bridging Together Theoretical and Experimental Perspectives in Single-Atom Alloys for Electrochemical Ammonia Production," *Small* 20 (2024): 2308084, https://doi.org/10.1002/smll.202308084.

10. M. H. Ward, R. R. Jones, J. D. Brender, et al., "Drinking Water Nitrate and Human Health: An Updated Review," *International Journal of Environmental Research and Public Health* 15 (2018): 1557, https://doi.org/10.3390/ijerph15071557.

11. S. Meng, Y. Ling, M. Yang, et al., "Recent Research Progress of Electrocatalytic Reduction Technology for Nitrate Wastewater: A Review," *Journal of Environmental Chemical Engineering* 11 (2023): 109418, https://doi.org/10.1016/j.jece.2023.109418.

12. Y. Fernández-Nava, E. Marañón, J. Soons, and L. Castrillón, "Denitrification of Wastewater Containing High Nitrate and Calcium Concentrations," *Bioresource Technology* 99 (2008): 7976–7981, https://doi.org/10.1016/j.biortech.2008.03.048.

13. C. Sun, H. Yin, X. Xing, Y. Lv, W. Xiong, and H. Li, "Effects of Different Alcohol Solvents on the Micromorphology of MnMoO4 and Their Electrocatalytic Performance in Ammonia Synthesis," *Industrial & Engineering Chemistry Research* 64 (2025): 8759–8767, https://doi.org/10.1021/acs.iecr.5c00474.

14. W. Zhang, T. Wang, X. Xing, et al., "Effects of Surfactants on the Size Distribution and Electrocatalytic Nitrite Reduction of Uniformly Dispersed Au Nanoparticles," *ACS Sustainable Chemistry and Engineering* 12 (2024): 10313–10324, https://doi.org/10.1021/acssuschemeng.3c07687.

15. Y. Wang, J. Li, X. Xing, et al., "Challenges and Breakthroughs in Single-Atom Catalysts for Electrocatalytic Nitrate Reduction to Ammonia," *ACS Sustainable Chemistry and Engineering* 13 (2025): 6875–6899, https://doi.org/10.1021/acssuschemeng.5c01249.

16. K. Flores, G. A. Cerrón-Calle, C. Valdes, et al., "Outlining Key Perspectives for the Advancement of Electrocatalytic Remediation of Nitrate from Polluted Waters," *ACS ES&T Engineering* 2 (2022): 746–768, https://doi.org/10.1021/acsestengg.2c00052.

17. R. Picetti, M. Deeney, S. Pastorino, et al., "Nitrate and Nitrite Contamination in Drinking Water and Cancer Risk: A Systematic Review with Meta-Analysis," *Environmental Research* 210 (2022): 112988, https://doi.org/10.1016/j.envres.2022.112988.

18. E. Rauh and S. Hughes, "Collaboration for Source Water Protection in the United States: Community Water Systems Engagement in Nitrate Pollution Reduction," *WIREs Water* 11 (2024): e1682, https://doi.org/10.1002/wat2.1682.

19. D. Liu, L. Qiao, S. Peng, et al., "Recent Advances in Electrocatalysts for Efficient Nitrate Reduction to Ammonia," *Advanced Functional Materials* 33 (2023): 2303480, https://doi.org/10.1002/adfm.202303480.

20. I. M.ul Hasan, N. Xu, Y. Liu, M. Z. Nawaz, H. Feng, and J. Qiao, "Noble and Non-Noble Metal Based Catalysts for Electrochemical Nitrate Reduction to Ammonia: Activity, Selectivity and Stability," *Electrochemical Energy Reviews* 7 (2024): 36, https://doi.org/10.1007/s41918-024-00236-7.

21. Y. Xiong, Y. Wang, J. Zhou, F. Liu, F. Hao, and Z. Fan, "Electrochemical Nitrate Reduction: Ammonia Synthesis and the Beyond," *Advanced Materials*," 36 (2024): 2304021, https://doi.org/10.1002/adma.202304021.

22. J. Zhang, T. Quast, B. Eid, et al., "In-Situ Electrochemical Reconstruction and Modulation of Adsorbed Hydrogen Coverage in Cobalt/Ruthenium-Based Catalyst Boost Electroreduction of Nitrate to Ammonia," *Nature Communications* 15 (2024): 8583, https://doi.org/10.1038/s41467-024-52780-x.

23. B. Xu, D. Li, Q. Zhao, S. Feng, X. Peng, and P. K. Chu, "Electrochemical Reduction of Nitrate to Ammonia Using Non-Precious Metal-Based Catalysts," *Coordination Chemistry Reviews* 502 (2024): 215609, https://doi.org/10.1016/j.ccr.2023.215609.

24. F. Rehman, M. Delowar Hossain, A. Tyagi, D. Lu, B. Yuan, and Z. Luo, "Engineering Electrocatalyst for Low-Temperature N2 Reduction to Ammonia," *Materials Today* 44 (2021): 136–167, https://doi.org/10.1016/j.mattod.2020.09.006.

25. A. Wang, J. Ye, Y. Yang, G. He, and H. Chen, "Recent Advances in Nickel-Based Catalysts for Electrochemical Nitrate Reduction to Ammonia," *Journal of Industrial and Engineering Chemistry* 132 (2024): 66–79, https://doi.org/10.1016/j.jiec.2023.11.039.

26. Y. Dang, R. Zhang, S. Ren, et al., "Balancing Active Hydrogen and NO2− for Interfacial Tandem Nitrate Electrocatalysis to Ammonia," *Chemical Engineering Journal* 520 (2025): 166370, https://doi.org/10.1016/j.cej.2025.166370.

27. Z. Zhang, M. Liu, B. Ge, et al., "In-Situ Reconstructed Cu/NiO Nanosheets Synergistically Boosting Nitrate Electroreduction to Ammonia," *Chinese Chemical Letters* 36 (2025): 110657, https://doi.org/10.1016/j.cclet.2024.110657.

28. Y. Bahari Molla Mahaleh, S. K. Sadrnezhaad, and D. NiO. Hosseini, "Nanoparticles Synthesis by Chemical Precipitation and Effect of Applied Surfactant on Distribution of Particle Size," *Journal of Nanomaterials* 2008 (2008): 470595, https://doi.org/10.1155/2008/470595.

29. L. Liu, Z. Wang, J. Zhang, O. Ruzimuradov, K. Dai, and J. Low, "Tunable Interfacial Charge Transfer in a 2D–2D Composite for Efficient Visible-Light-Driven CO2 Conversion," *Advanced Materials* 35 (2023): 2300643, https://doi.org/10.1002/adma.202300643.

30. J. Li, X. Yu, W. Xue, L. Nie, H. Huang, and C. Zhong, "Engineering the Direct Z-Scheme Systems over Lattice Intergrown of MOF-on-MOF for Selective CO2 Photoreduction to CO," *AIChE Journal* 69 (2023): e17906, https://doi.org/10.1002/aic.17906.

31. J. Lei, N. Zhou, S. Sang, S. Meng, J. Low, and Y. Li, "Unraveling the Roles of Atomically-Dispersed Au in Boosting Photocatalytic CO2 Reduction and Aryl Alcohol Oxidation," *Chinese Journal of Catalysis* 65 (2024): 163–173, https://doi.org/10.1016/S1872-2067(24)60109-9.

32. X. Li, B. Y. Guan, S. Gao, and X. W. Lou, "A General Dual-Templating Approach to Biomass-Derived Hierarchically Porous Heteroatom-Doped Carbon Materials for Enhanced Electrocatalytic Oxygen Reduction," *Energy & Environmental Science* 12 (2019): 648–655, https://doi.org/10.1039/c8ee02779j.

33. P. Zhang, W. Xiong, and M. Zhou, "Effect of Nickel Oxide Morphology on the Nitrogen Electrochemical Reduction Reaction," *Nano Materials Science* 2 (2020): 353–359, https://doi.org/10.1016/j.nanoms.2020.03.002.

34. S. Pujiastuti and H. Onggo, "Effect of Various Concentration of Sulfuric Acid for Nafion Membrane Activation on the Performance of Fuel Cell," *AIP Conference Proceedings* 1711 (2016): 060006, https://doi.org/10.1063/1.4941639.

35. J. J. Giner-Sanz, G. Leverick, V. Pérez-Herranz, and Y. Shao-Horn, "Optimization of the Salicylate Method for Ammonia Quantification from Nitrogen Electroreduction," *Journal of Electroanalytical Chemistry* 896 (2021): 115250, https://doi.org/10.1016/j.jelechem.2021.115250.

36. Y. Li, X. Xie, J. Liu, M. Cai, J. Rogers, and W. Shen, "Synthesis of α-Ni(OH)2 with Hydrotalcite-Like Structure: Precursor for the Formation of NiO and Ni Nanomaterials with Fibrous Shapes," *Chemical Engineering Journal* 136 (2008): 398–408, https://doi.org/10.1016/j.cej.2007.06.001.

37. M. Rajamathi, G. N. Subbanna, and P. V. Kamath, "On the Existence of a Nickel Hydroxide Phase Which Is Neither α nor β," *Journal of Materials Chemistry* 7 (1997): 2293–2296, https://doi.org/10.1039/a700390k.

38. M. Vidotti, R. P. Salvador, E. A. Ponzio, and S. I. Córdoba de Torresi, "Mixed Ni/Co Hydroxide Nanoparticles Synthesized by Sonochemical Method," *Journal of Nanoscience and Nanotechnology* 7 (2007): 3221–3226, https://doi.org/10.1166/jnn.2007.651.

39. S. Jahangiri and N. J. Mosey, "Molecular Structure and Interactions of Water Intercalated in Nickel Hydroxide," *Physical Chemistry Chemical Physics* 20 (2018): 11444–11453, https://doi.org/10.1039/C8CP00070K.

40. P. Dubey, N. Kaurav, R. S. Devan, G. S. Okram, and Y. K. Kuo, "The Effect of Stoichiometry on the Structural, Thermal and Electronic Properties of Thermally Decomposed Nickel Oxide," *RSC Advances* 8 (2018): 5882–5890, https://doi.org/10.1039/c8ra00157j.

41. S. Bhanuchandar, G. Vinothkumar, P. Arunkumar, M. Sribalaji, A. K. Keshri, and K. S. Babu, "Unravelling the Role of Cationic Ni2+ Vacancies and Ni3+ Ions in Non-Stoichiometric NiO: Breakdown of Anti-Ferromagnetic Ordering and Large Exchange Bias," *Journal of Materials Science* 582 (2023): 13136–13153, https://doi.org/10.1007/s10853-023-08853-1.

42. M. Steimecke, G. Seiffarth, C. Schneemann, F. Oehler, S. Förster, and M. Bron, "Higher-Valent Nickel Oxides with Improved Oxygen Evolution Activity and Stability in Alkaline Media Prepared by High-Temperature

Treatment of $Ni(OH)_2$," *ACS Catalysis* 10 (2020): 3595–3603, https://doi.org/10.1021/acscatal.9b04788.

43. M. Thommes, K. Kaneko, A. V. Neimark, et al., "Physisorption of Gases, with Special Reference to the Evaluation of Surface Area and Pore Size Distribution (IUPAC Technical Report," *Pure and Applied Chemistry* 87 (2015): 1051–1069, https://doi.org/10.1515/pac-2014-1117.

44. M. Thommes, "Physical Adsorption Characterization of Nanoporous Materials," *Chemie Ingenieur Technik* 82 (2010): 1059–1073, https://doi.org/10.1002/cite.201000064.

45. V. G. Baldovino-Medrano, V. Niño-Celis, and R. Isaacs Giraldo, "Systematic Analysis of the Nitrogen Adsorption–Desorption Isotherms Recorded for a Series of Materials Based on Microporous–Mesoporous Amorphous Aluminosilicates Using Classical Methods," *Journal of Chemical and Engineering Data* 68 (2023): 2512–2528, https://doi.org/10.1021/acs.jced.3c00257.

46. N. Mironova-Ulmane, A. Kuzmin, I. Sildos, L. Puust, and J. Grabis, "Magnon and Phonon Excitations in Nanosized NiO," *Latvian Journal of Physics and Technical Sciences* 56 (2019): 61–72, https://doi.org/10.2478/lpts-2019-0014.

47. P. Bose, S. Ghosh, S. Basak, and M. K. Naskar, "A Facile Synthesis of Mesoporous NiO Nanosheets and Their Application in CO Oxidation," *Journal of Asian Ceramic Societies* 4 (2016): 1–5, https://doi.org/10.1016/j.jascer.2016.01.006.

48. J. Qiu, T. H. Nguyen, S. Kim, et al., "I.-S. Two-Dimensional Correlation Spectroscopy Analysis of Raman Spectra of NiO Nanoparticles," *Spectrochimica Acta Part A, Molecular and Biomolecular Spectroscopy* 280 (2022): 121498, https://doi.org/10.1016/j.saa.2022.121498.

49. A. Sunny and K. Raman Balasubramanian, "Spectral Probe on Size-Dependent Surface Optical Phonon Modes and Magnon Properties of NiO Nanoparticles," *The Journal of Physical Chemistry C* 124 (2020): 12636–12644, https://doi.org/10.1021/acs.jpcc.0c02638.

50. M. C. Biesinger, B. P. Payne, A. P. Grosvenor, L. W. M. Lau, A. R. Gerson, and R. S. C. Resolving Smart, "Surface Chemical States in XPS Analysis of First Row Transition Metals, Oxides and Hydroxides: Cr, Mn, Fe, Co and Ni," *Applied Surface Science* 257 (2011): 2717–2730, https://doi.org/10.1016/j.apsusc.2010.10.051.

51. G. Nguila Inari, M. Petrissans, J. Lambert, J. J. Ehrhardt, and P. Gérardin, "XPS Characterization of Wood Chemical Composition after Heat-Treatment," *Surface and Interface Analysis* 38 (2006): 1336–1342, https://doi.org/10.1002/sia.2455.

52. H. W. Nesbitt, D. Legrand, and G. M. Bancroft, *Interpretation of Ni2p XPS Spectra of Ni Conductors and Ni Insulators*.

53. M. C. Biesinger, L. W. M. Lau, A. R. Gerson, and R. S. C. Smart, "The Role of the Auger Parameter in XPS Studies of Nickel Metal, Halides and Oxides," *Physical Chemistry Chemical Physics* 14 (2012): 2434–2442, https://doi.org/10.1039/c2cp22419d.

54. N. Weidler, J. Schuch, F. Knaus, et al., "X-Ray Photoelectron Spectroscopic Investigation of Plasma-Enhanced Chemical Vapor Deposited NiOx, NiOx(OH)y, and CoNiOx(OH)y: Influence of the Chemical Composition on the Catalytic Activity for the Oxygen Evolution Reaction," *Journal of Physical Chemistry C* 121 (2017): 6455–6463, https://doi.org/10.1021/acs.jpcc.6b12652.

55. A. R. Blume, W. Calvet, A. Ghafari, T. Mayer, A. Knop-Gericke, and R. Schlögl, "Structural and Chemical Properties of NiOx Thin Films: The Role of Oxygen Vacancies in NiOOH Formation in a H2O Atmosphere," *Physical Chemistry Chemical Physics* 25 (2023): 25552–25565, https://doi.org/10.1039/d3cp02047a.

56. K. O. Egbo, C. P. Liu, C. E. Ekuma, and K. M. Vacancy Yu, "Defects Induced Changes in the Electronic and Optical Properties of NiO Studied by Spectroscopic Ellipsometry and First-Principles Calculations," *Journal of Applied Physics* 128 (2020): 135705, https://doi.org/10.1063/5.0021650.

57. N. Pirrone, S. Garcia-Ballesteros, J. Amici, M. Castellino, S. Hernández, and F. Bella, "Chemometrics-Boosted Protocols for Effortless Evaluation of Factors Affecting the Electrochemical Nitrate Reduction to Ammonia," *Journal of Energy Chemistry* 107 (2025): 599–611, https://doi.org/10.1016/j.jechem.2025.03.072.

58. X. Yang, Y. Cui, Y. Qi, et al., "Self-Supporting NiO-Coated Activated Carbon Nanofibers Based on Atomic Layer Deposition for Supercapacitor," *Journal of Alloys and Compounds* 958 (2023): 170513, https://doi.org/10.1016/j.jallcom.2023.170513.

59. S. Chen, R. Tao, J. Tu, et al., "Performance Flexible Lithium-Ion Battery Electrodes: Ion Exchange Assisted Fabrication of Carbon Coated Nickel Oxide Nanosheet Arrays on Carbon Cloth," *Advanced Functional Materials* 31(2021): 2101199, https://doi.org/10.1002/adfm.202101199.

60. R. Kostecki and F. McLarnon, "Electrochemical and In Situ Raman Spectroscopic Characterization of Nickel Hydroxide Electrodes: I. Pure Nickel Hydroxide," *Journal of the Electrochemical Society* 144 (1997): 485–493, https://doi.org/10.1149/1.1837437.

Supporting Information

Additional supporting information can be found online in the Supporting Information section. **Supporting Fig. S1:** Synthetic protocol of sample W100 (a) and sample E100 (b). **Supporting Fig. S2:** Comparison between CA and LSV measurements for (a) E32 and (b) E100 samples. In Test 1, the electrodes were fabricated using an ink formulated with butanol as the dispersion medium and subjected to ultrasonication at 60% of the maximum amplitude. In Test 2, the ink was prepared using isopropanol as the solvent and sonicated at 85% amplitude prior to electrode deposition. **Supporting Fig. S3:** Three CA replicates performed under identical conditions with W100 as the active material, highlighting the variability in behavior and the limited reproducibility of the results. **Supporting Table S1:** Ammonia production, FE%, and catalyst loading values reported for different replicates with E32 and E100 samples, prepared using two distinct ink preparation methods. **Supporting Table S2:** Ammonia production, FE%, and catalyst loading values reported for different replicates with W100 sample.